Appl. Phys. B (2015) 121:439–451
DOI 10.1007/s00340-015-6251-5

Applied Physics B
Lasers and Optics

Experimental evidence of temporal and spatial incoherencies of Q-switched Nd:YAG nanosecond laser pulses

R. Diaz[1,2] · R. Courchinoux[1] · J. Luce[1] · C. Rouyer[1] · J.-L. Rullier[1] · J.-Y. Natoli[2] · L. Lamaignère[1]

Received: 31 July 2015 / Accepted: 14 October 2015 / Published online: 30 October 2015

Abstract Seeded nanosecond Q-switched Nd:YAG lasers working with an unstable resonator and a variable reflectivity mirror are widely used, for they represent useful sources for stable and repeatable light–matter interaction experiments. Moreover, in most setups, the fundamental wavelength is converted to higher harmonics. When the injection seeder is turned off, random longitudinal mode beating occurs in the cavity, resulting in strong variations of the temporal profile of the pulses. The generated spikes can then be ten times higher than the maximum of equivalent seeded pulses. This strong temporal incoherence is shown to engender spatial incoherence in the focal plane of such unseeded pulses leading to an instantaneous angular displacement of tens of µrad. This effect is even more pronounced after frequency conversion.

1 Introduction

Flashlamp-pumped, Q-switched Nd:YAG lasers generate nanosecond light pulses with energy of several joules at repetition rates up to 100 Hz that are useful sources for light–matter interaction experiments. For high-energy extraction, the use of unstable resonator is widely spread, for they enhance gain efficiency [1]. Unstable resonators are made up of two plane mirrors and result in multimode transversal cavity. On the one hand, single transversal mode operation of unstable resonator was made possible thanks to highly selective variable reflectivity mirror (VRM) at the output coupler [2]. However, previous studies have shown that such cavities may still generate a beam of poor spatial quality [3, 4]. On the other hand, the selection of a single longitudinal mode of an unstable resonator is possible by injection locking technics [5] and permits the generation of repeatable near-Gaussian pulses with great temporal coherence. However, incoherent light with a short coherence time is of interest for coherent spectroscopy [6–8] and for many other applications, such as tomography in random media [9], and for the use of spatial incoherence in optical spatial smoothing techniques for uniform irradiation in plasma physics [10–12]. Therefore, temporal incoherence induced by longitudinal mode beating in unseeded laser cavities remains a subject of wide interest.

In the present work, we quantify the spatial incoherence at the output of an unseeded Q-switched Nd:YAG laser by means of picosecond streak cameras at the fundamental wavelength and the third harmonic since in most setups the fundamental wavelength of the laser system is converted to higher harmonics thanks to nonlinear crystals [6, 7, 10]. Spatial incoherence results in instantaneous angular displacement of few tens of µrad in the focal plane of the beam. This observation involves that the temporal incoherence of unseeded pulses does systematically induce spatial incoherence. Moreover, we empirically demonstrate that this effect is more pronounced after frequency tripling through nonlinear crystals. We propose to explain the experimental tendency with the occurrence of Kerr effect in the Nd:YAG rods. In that matter, we first need to statistically characterize the temporal characteristics of unseeded pulses with measuring the spectral and temporal profiles by means of high-resolution spectrometer and photodiode, respectively. Then, calculations are made to reinforce the

✉ R. Diaz
romaindiaz.rd@gmail.com

[1] CEA Cesta, 15 avenue des sablières, CS 60001, 33116 Le Barp Cedex, France

[2] CNRS, Ecole Centrale Marseille, Institut Fresnel, UMR 7249, Aix Marseille Université, 13013 Marseille, France

reliability of experimental acquisitions of the temporal profiles. Since streak cameras are used as key diagnostics for spatial incoherence, the acquisitions they provide are first compared to the signals of the photodiodes so as to strengthen their reliability. Finally, thanks to this preparatory metrology, the picosecond streak cameras allow the measurement of the spatial incoherence in the focal plane of the beam at the fundamental wavelength and after frequency tripling.

2 Experimental setup

2.1 The Q-switched Nd:YAG laser

The subject of our experimental investigations is a Q-switched Nd:YAG laser (Spectra-Physics Quanta-Ray PRO-350) working at 10 Hz made of an unstable resonator which consists in a plane mirror mounted on a piezoelectric cell, a Pockels cell, two Nd:YAG rods and a VRM as the output coupler. An integrated seed laser (Spectra-Physics Model 6350), which wavelength is centered at 1064.4 nm, delivers enough power to overcome the noise induced by spontaneous emission [5], whereas random longitudinal mode beating occurs when it is turned off. The optical length of the resonator is $L = 820$ mm, and the free spectral range is $c/2L$=183 MHz. The two-rod amplifiers are 9.5 mm in diameter and 15 cm long. After building up, the pulsed light passes through the two other rods of Nd:YAG of 12.7 mm in diameter and 15 cm long. This laser delivers a beam of 12 mm in diameter. The outgoing wavelength can either be 1064 nm (1ω) or 355 nm (3ω) after passing through a type I KDP crystal and a type II KDP crystal that permit the generation of the second and third harmonic, respectively. The energy of the pulses can be 2 J at 1ω and 700 mJ at 3ω. The photograph of the laser with the different elements is given in Fig. 1.

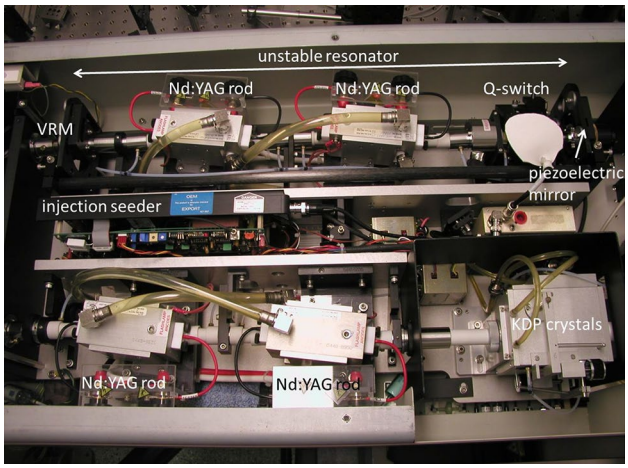

Fig. 1 Photograph of the Nd:YAG laser with the different components

2.2 The metrology

Figure 2 represents a scheme of the experimental setup with the positions of all the devices brought into operation for the metrology of the pulses. A beam shutter ensures the selection of a single shot for the experiments. At the exit of the laser described in Fig. 1, the use of the transmitted part of a high-reflective mirror makes possible the sufficient attenuation of the energy in order to illuminate the different diagnostics. This drastically attenuates the outgoing flux of the laser. The half-wave plate coupled to the polarizer permits the control of the energy incoming on the diagnostics. The reflected part of the beam on the first mirror goes on a calorimeter that ensures the measurement of the total energy of each pulse.

2.2.1 High-resolution grating spectrometer

The object of the measurement of the spectrum is to provide a lower limit for the bandwidth of the temporal diagnostics used later. Moreover, the use of a high-resolution spectrometer provides a realistic image of the spectral information contained in both SLM and MLM pulses and allows the comparison of the functioning of the laser in both regimes. In Fig. 2, the attenuated beam reflects on a transport mirror and passes through an 8-m focusing lens. Then, a 50–50 beam splitter separates the beam. The reflected part ends up on a high-resolution grating spectrometer [13] that uses three reflecting gratings, noted grating 1, grating 2 and grating 3. After passing through the collimating lens of the spectrometer, the beam undergoes four reflections of different order of diffraction on the three different gratings. The first reflection is on grating 1, the second on grating 2, the third on grating 3 and the fourth on grating 1. The great dispersion of the gratings permits to translate spectral information into a one-dimensional image on a CCD camera which is perpendicular to the lines of the gratings. In this configuration, the resulting acquisition has a resolution of 1 GHz at 1ω. This resolution depends on the number of lines that are illuminated on the gratings. The more groves the beam sees, the higher the resolution is.

2.2.2 Ultrafast fiber-coupled photodiodes

High-resolution temporal diagnostics are implemented in this setup in order to fully characterize the temporal

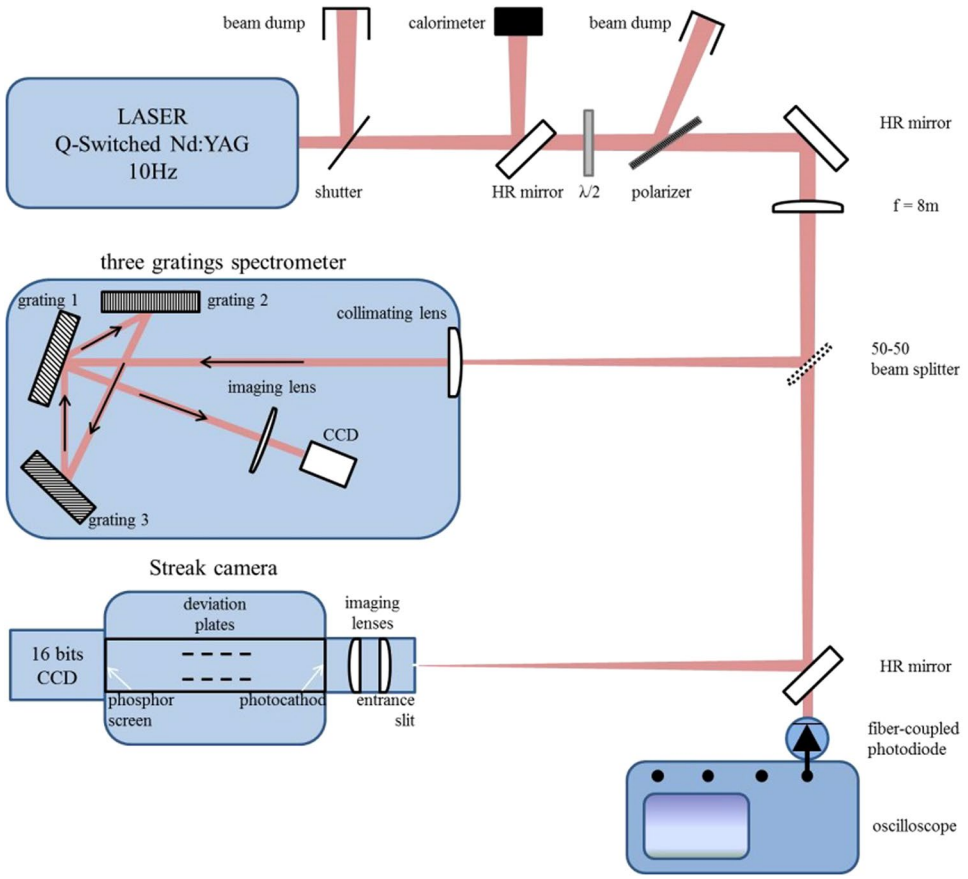

Fig. 2 Schematic representation of the experimental setup

structure of the pulses. Therefore, the transmitted part of the beam after the 50–50 beam splitter is reflected on a high-reflective mirror. The fraction of the pulse that is transmitted is injected into a fiber-coupled photodiode. At 1ω (respectively 3ω), the bandwidth of the photodiode is 45 GHz (respectively 40 GHz). The injection is ensured by means of a microscope objective 10× with a numerical aperture of 0.26 that collects the entirety of the beam and focuses it into a single-mode fiber. The photodiode is directly plugged on a 33-GHz bandwidth oscilloscope (Tektronix DSA73304D). Finally, the total resolution of the acquisitions is 30 ps with a sample rate of 100 GS/s at both wavelengths. No cable is used here so as to preserve the maximum bandwidth from the photodiode. Indeed, most cables impose a limitation on the temporal resolution because of the strong attenuation they induce at high frequencies.

2.2.3 Picosecond streak cameras

In order to measure and quantify the spatial incoherence, the reflected part of the beam goes onto the horizontal slit of a streak camera Thompson TSN 506 (respectively ARP TRD3) positioned in the focal plane of the 1ω (respectively 3ω) beam. This type of apparatus provides high temporal resolution [14]. Moreover, it provides a spatially resolved acquisition of the temporal profile, whereas the fiber-coupled photodiodes used here give a signal that spatially integrates the whole beam. The functioning of the streak camera is similar to the one described in Ref. [15]. The entrance slit is imaged on a photocathode that ensures the conversion of photons into electrons. The generated photoelectrons deflected vertically thanks to high-voltage deviation plates into a vacuum tube. Then, the electrons at the output of the streak tube impact a phosphor screen. The photoluminescence generated at the phosphor screen is imaged by a 16-bit CCD sensor, which chip is cooled to −20 °C, thanks to a Peltier element. This CCD sensor provides a two-dimensional spatiotemporal image of the laser pulse with a spatial resolution of 10 µm. The space and time coordinates are not altered during the flight of the electrons in the tube. The time coordinate is perpendicular to the slit. The dynamic range and the intensity-dependent time resolution of the streak camera have been taken into account in order to avoid space charge and accumulative saturation effects [15, 16].

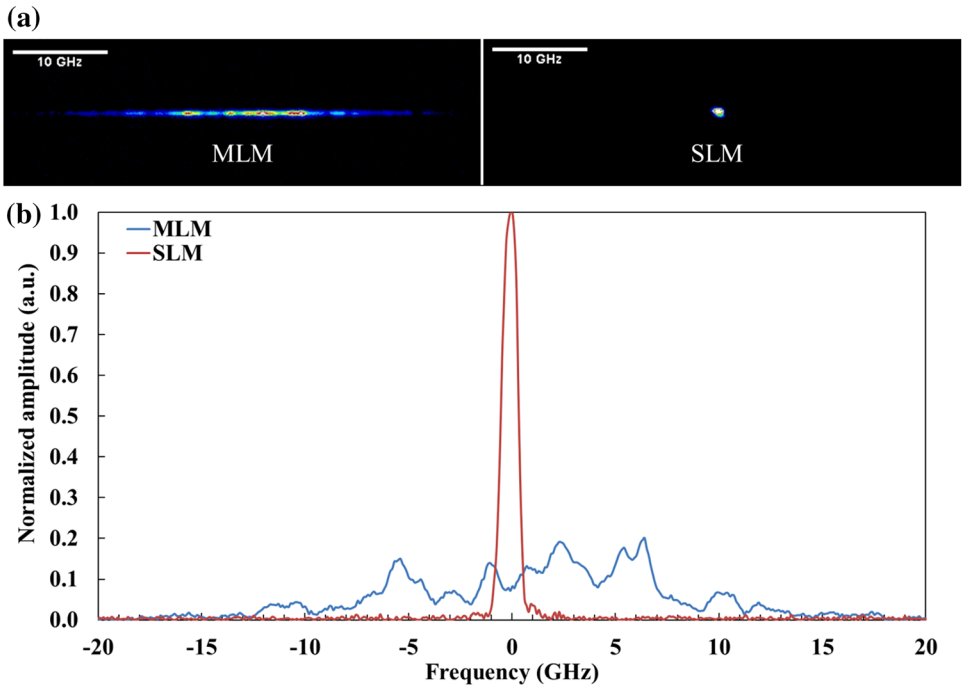

Fig. 3 Typical spectral profiles obtained in the MLM and SLM regimes at 1ω. **a** Raw images in both regimes of the spectrometer. **b** Spectral power density in both regimes integrated with the same power. The zero corresponds to the center wavelength 1064.4 nm. The resolution of the acquisitions is 1 GHz

3 Quantification of the temporal incoherence of unseeded laser pulses

3.1 Experimental results

In this part, we experimentally investigate the spectral and temporal dynamics of the pulses in the both SLM and MLM regimes. As mentioned earlier, the measurement of the spectrum provides the knowledge of the spectral bandwidth of the pulses in both regimes. This measurement is necessary to acquire the temporal profile of the pulses with the different diagnostics. High-resolution photodiodes are used alongside with picosecond streak cameras for the demonstration of the reliability of the acquisitions. In this section, streak cameras are used to acquire the temporal characteristics of the pulses only.

3.1.1 Measurement of the 20 GHz spectral width of the pulses

Time-integrated acquisitions of the spectrum are performed by means of the grating spectrometer described in Fig. 2 [13]. An example of MLM and SLM spectra is reported in Fig. 3. The images from the CCD camera presented in Fig. 3a clearly show the fundamental differences between the two modal configurations. In the MLM image, the position and magnitude of hot spots depend on the random phases of the modes. In the SLM image of Fig. 3a, the single spot traduces the single mode operated by the injection seeder. In Fig. 3b, the MLM spectral profile is strongly modulated and random shot to shot. The power of MLM pulse is spread over different wavelengths randomly. On the contrary, the near-Gaussian SLM spectrum is smooth and repeatable shot to shot over hundreds of thousands of pulses. Both profiles are normalized with the same power. In our laser, the optical length of the laser cavity is about 820 mm. As a consequence, the spacing of the frequency spikes in the MLM spectrum can be as short as 183 MHz, but is not well resolved with the spectrometer as shown in Fig. 3b. Moreover, in the SLM regime, the width of the observed dot in the acquisition presented in Fig. 3b should be as well $\leq$183 MHz instead of 1 GHz which is the limit of this spectrometer. The two spectral power density profiles in Fig. 3 clearly show the different spectral behaviors obtained in the two regimes. The spectral differences between the SLM and MLM spectra are conserved after frequency tripling in the crystals. That means the picture will be the same when comparing the shape of the spectral power densities. Therefore, the measurement of the spectrum has not been made at 3ω.

Hundred different acquisitions have been performed in the MLM regime with the grating spectrometer. The normalized sum over all the acquisitions is reported in Fig. 4. The full width at half maximum (FWHM) of the near-Gaussian spectral gain of the Nd:YAG is around 20 GHz. This value represents the spectral width of the laser gain narrowing of neodymium ions in the YAG lattice. This gives the limit of the bandwidth that one needs to measure accurately the temporal profile of the MLM laser pulses at 1ω. After frequency tripling, the overall Gaussian FWHM

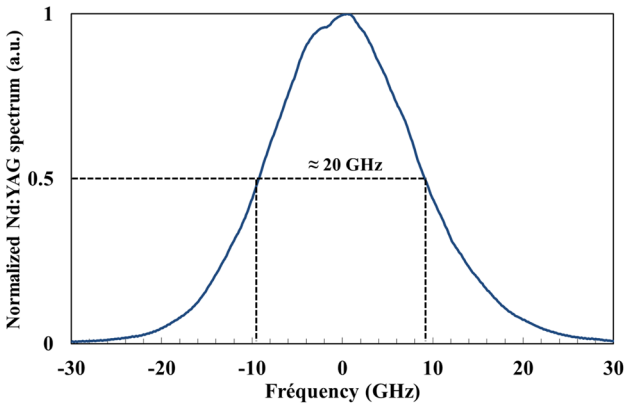

Fig. 4 Measured near-Gaussian spectral gain of the Nd:YAG laser over 100 acquisitions in the MLM regime. The zero corresponds to the center wavelength 1064.4 nm

of the spectrum is around 30 GHz [17]. This enlargement of the spectrum is mostly due to saturation of the frequency conversion in the crystals [18]. In the next part, acquisitions of the temporal profile of the pulses at both wavelength and in the two spectral configurations are presented and discussed.

3.1.2 Quantification of the temporal incoherence of the pulses

As described earlier, acquisitions of the space-integrated temporal profiles at 1ω (respectively 3ω) are performed by means of a fiber-coupled photodiode. At both wavelengths, the bandwidth of the detectors is larger than the width of the spectrum in the MLM regime. Typical MLM and SLM temporal profiles are reported in Fig. 5. For each wavelength, the two signals have been integrated with the same power and are thus comparable. At 1ω (cf. Fig. 5a), in both SLM and MLM cases, the duration of the pulse is governed by the lifetime of a photon in the cavity. As the lifetime of a photon in the cavity is the same in both regimes, the duration of the pulses is the same whatever the longitudinal mode configuration. In our case, the equivalent duration is about 9 ns at 1ω. After frequency conversion, the equivalent duration of the pulses is 7 ns (Fig. 5b). This is due to frequency conversion that shortens the duration of the pulses [18], for the feet of the temporal Gaussian are not converted.

When considering the temporal structure of MLM pulses, the random spectral fluctuations due to longitudinal mode beating induce strong variation in the position and magnitude of the temporal spikes. Moreover, temporal spikes at 1ω can be as short as 40 ps FWHM, and an almost systematical return-to-zero is observed between two adjacent spikes [19]. The same return-to-zero is observed at 3ω, and the spike can be shorter as 30 ps for the same reason that SLM pulses are shorter at 3ω than at 1ω. This is a direct consequence of the spectrum being slightly wider after frequency conversion.

Twenty thousand MLM 1ω shots have been acquired with the photodiode in order to quantify the statistical fluctuations of the magnitude of the temporal spikes. For each signal, the equivalent SLM pulse is calculated by smoothing with a 183-MHz bandwidth filter. Then, the ratio of the highest spike I_{max} on the maximum of the equivalent SLM pulse I_0 is calculated for each MLM shot. In Fig. 6, the number of counts of I_{max}/I_0 is reported. The mean value is 4.6, and the maximum I_{max} is ten times greater than the equivalent I_0 of the considered pulse. The dispersion, defined as the standard deviation over the mean value, is about 22 %.

In this part, the streak camera (Thompson TSN 506) has been used for the temporal characterization of the MLM pulses at 1ω. The acquisitions of the streak camera are treated only on their time coordinate. This allows the evaluation of a part of the temporal profile. As a comparison, a

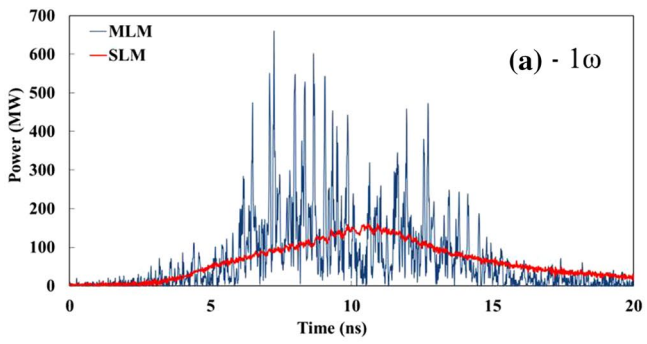

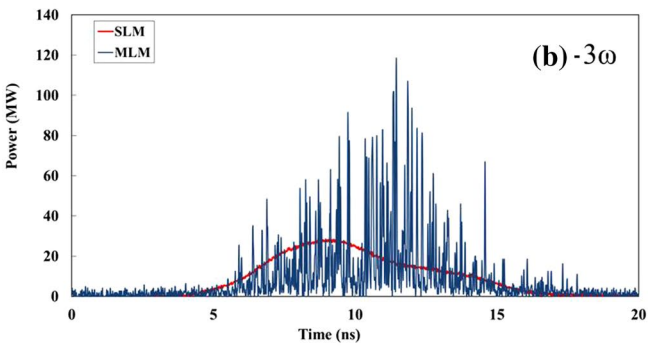

Fig. 5 Typical space-integrated temporal profiles obtained with the fiber-coupled photodiode in the MLM (*blue line*) and SLM (*red line*) regimes at 1ω (**a**) and 3ω (**b**). The bandwidth of the acquisitions is 33 GHz. At both wavelengths, SLM and MLM signals have been integrated with the same power

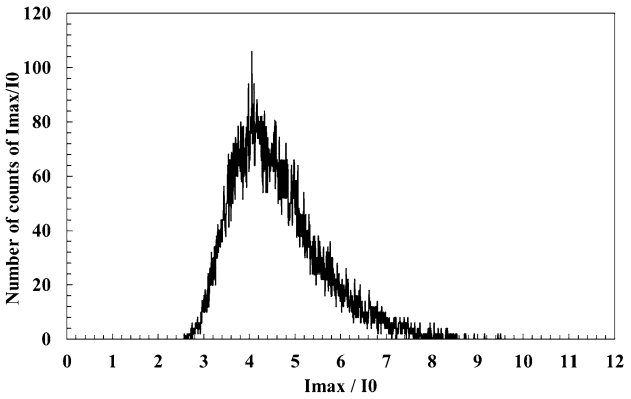

Fig. 6 Number of counts of the ratio of the value of the highest spike I_{max} on the maximum I_0 of their equivalent SLM pulse over 20,000 1ω MLM pulses

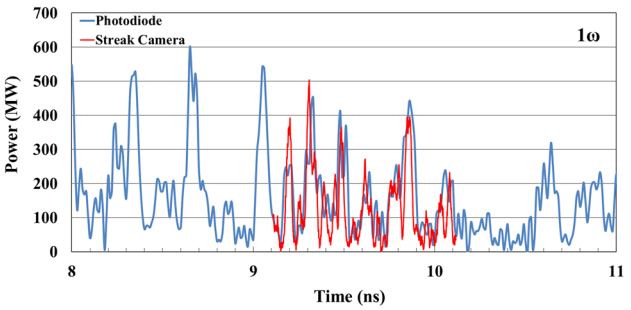

Fig. 7 Comparison between the temporal profiles acquired with the streak camera and with the photodiode at 1ω

streak camera acquisition is superimposed on a photodiode signal in Fig. 7. This allows us to verify that the two apparatuses used in the experiment are in good agreement. The caliber of the acquisitions is 55 ps/mm on the whole phosphor screen with an opening of the slit of 100 µm. The pulse can thus be cut into slices of 5.5-ps duration. The resolution of the temporal acquisition is thus 11 ps. This corresponds to an equivalent bandwidth of about 90 GHz which is much larger than the width of the spectrum of the MLM pulses. The opening of the slit thus allows a better resolution than the one of the photodiode. However, at this resolution, the temporal length of the signal does not exceed a nanosecond due to the limited size of the CCD sensor that images the phosphor screen. The good agreement between the two acquisitions presented in Fig. 7 comforts us in the measurements that are made with the fiber-coupled photodiode. Indeed, both instruments give the same information since the acquisitions are resolved in time. That is to say, thanks to the knowledge of the spectral width, a bandwidth of 33 GHz is enough for the resolution of the MLM temporal profiles at 1ω. Moreover, the almost systematical return-to-zero between two adjacent spikes is here settled by the streak camera as well. Thanks to these observations, MLM pulses can thus be considered as a succession of picosecond pulses with random magnitudes. One can finally note the "sawtooth structure" of the 1ω MLM pulses.

The effect of frequency conversion on 1ω MLM pulses is now investigated. The structure and the statistics of temporal spikes of 3ω MLM pulses are presented. The same comparison between the photodiode and the streak camera has been performed. The FWHM of the spectrum evolves after frequency conversion, but stays within the bandwidth of the acquisition. A direct comparison of a streak camera acquisition and a photodiode signal is presented in Fig. 8. The streak camera is used with a caliber of 70 ps/mm with a slit of 100 µm. These two parameters engender a temporal resolution of 14 ps. This corresponds to an equivalent bandwidth of 70 GHz. The opening of the slit and the caliber thus allows a better resolution than the one of the photodiode. At this resolution, as said previously, the temporal signal length does not exceed a few nanoseconds due to the limited size of the CCD sensor that images the phosphor screen. At 3ω, we can also note the good agreement between the two signals. Again, this means that the temporal profiles of MLM pulses acquired thanks to the photodiode and the streak camera are resolved in time since the bandwidths of both instruments are larger than the spectral width of the pulses at 3ω. The spikes can be shorter at 3ω than at 1ω, and the troughs appear to be a bit larger at 3ω

Fig. 8 Comparison between the temporal profiles acquired with the streak camera and with the photodiode at 3ω

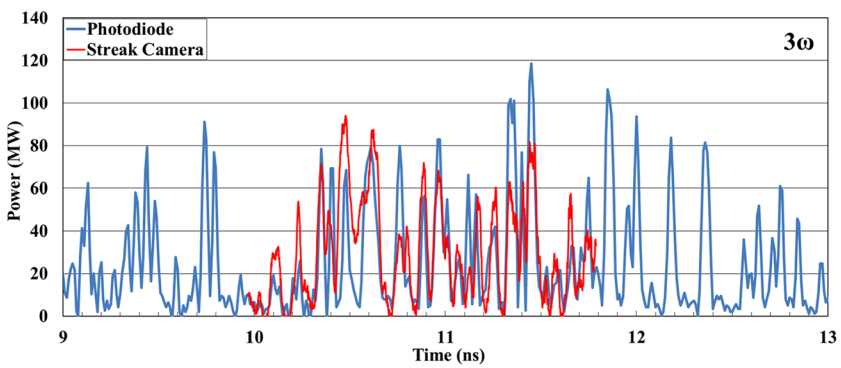

than at 1ω. The minimum FWHM duration of a spike is 30 ps. Again, this is a consequence of the mechanisms of frequency conversion. Indeed, a spike cannot be entirely converted through the crystals [18].

Now that the acquisitions are found to be reliable at 3ω, 20,000 shots have been acquired with the photodiode in order to statistically investigate the effects of frequency conversion on the magnitude of the spikes. The methodology is the same than that described earlier. In Fig. 9, the number of counts of I_{max}/I_0 is reported. The mean value is 3.7, and the maximum I_{max} is again ten times greater than the equivalent I_0 of the considered pulse. The dispersion is about 30 %. Two phenomena can explain the obtained differences between the histograms at 1ω and 3ω. First, due to the conversion efficiency, the highest spikes are on the average less high at 3ω than at 1ω. Secondly, mainly because of the saturation of frequency conversion in the crystals, the maxima I_{max}/I_0 are the same at the two wavelengths. Hence, the dispersion of the histograms is more important at 3ω than at 1ω.

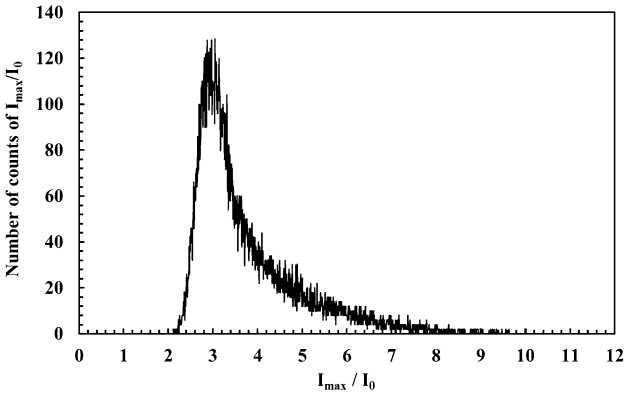

Fig. 9 Number of counts of the ratio of the value of the highest spike I_{max} on the maximum I_0 of their equivalent SLM pulse over 20,000 3ω MLM pulses

3.2 Numerical simulation of the spectral and temporal structure of the pulses

The measured results are compared with the predictions of a numerical simulation. The spectrum is calculated as a Gaussian of 20 GHz FWHM containing longitudinal modes spaced by 183 MHz. A result of the theoretical spectrum of MLM 1ω pulses is presented in Fig. 10. One can note that the discretization in the spectrum depicted here is not realistic and cannot be experimentally measured. Indeed, instabilities due to random spectral phases would alter this idealistic picture.

In order to generate a realistic temporal profile, a random phase is generated numerically for each mode contained in the narrowed gain. The duration of the pulse is set to 9 ns. An example of a generated temporal profile is shown in Fig. 11. For a given spectral profile, each temporal profile is random shot to shot. The almost systematical return-to-zero is also well reproduced by the simulation. The picture given by the acquisitions shown in the previous part is comforted thanks to this simulation.

The statistical fluctuations of MLM pulses are now simulated by generating 10,000 pulses. The spectrum of Fig. 10 is the same for each calculation. In order to quantify the variations in magnitude of the highest spikes, the ratios I_{max}/I_0 are calculated for each pulse where I_0 is the maximum of the equivalent SLM pulse. The methodology is the same than that described in the previous section. The result of this simulation is reported in Fig. 12. Highest I_{max}/I_0 is found to be equal to 10.5 and is as high as the maximum of the

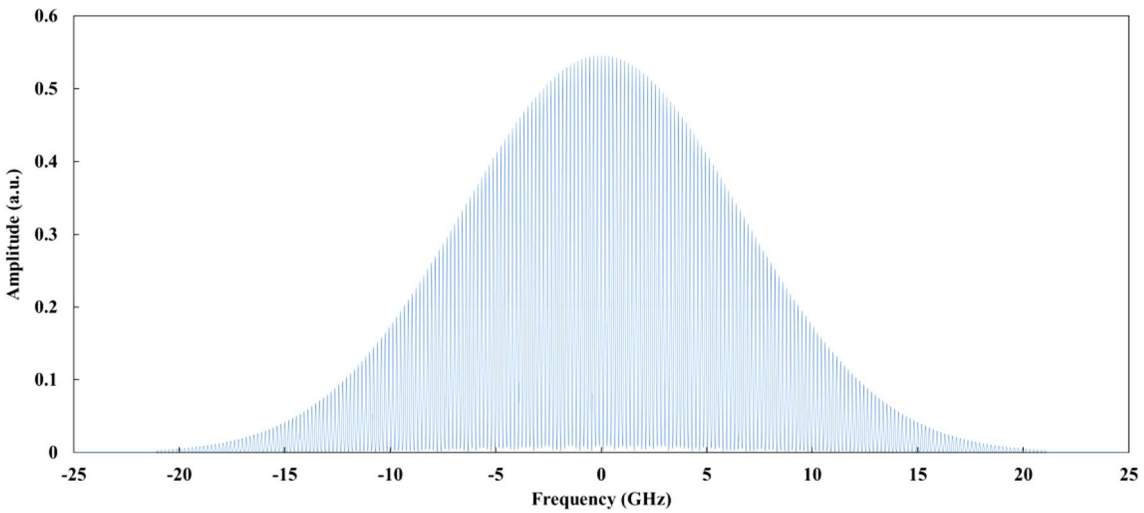

Fig. 10 Numerical calculation of the theoretical MLM spectral profile at 1ω

equivalent seeded pulse. The mean value is 4.7 in the simulation, and the dispersion calculated as the standard deviation over the mean value is 23 %. This simulation shows very good correlation with the experimental results depicted in Fig. 6.

Thanks to the great reliability of the calculations, our simulation program is used to calculate the focal spot in the MLM regime in the next part. Moreover, as the experimental 3ω MLM pulses do not show great difference with the 1ω MLM pulses, the frequency tripling is not numerically studied in this section. However, in the next section of the present work, the influence of nonlinear propagation in the crystals is investigated considering the spatial coordinate.

3.3 Conclusion

In this part, random longitudinal mode beating is shown to induce strong statistical fluctuations of the temporal profile characteristics. First, the measurement of the spectrum width permits the definition of the resolution of the apparatuses in order to measure accurately the temporal profile of the laser pulses. Therefore, the combination of a high-bandwidth photodiode and a fast streak camera leads to a better knowledge of the fine structure induced by random longitudinal mode beating. Moreover, the effect of frequency conversion is experimentally investigated. The good correlation between the acquisitions made with the photodiode and the streak cameras insists on the reliability of our metrology. At both wavelengths, a resolution of 33 ps with a sampling rate of 100 GS/s seems to be sufficient in resolving the temporal profile of MLM pulses.

The comparison between numerical simulation and experimental results shows very good agreement at 1ω. Indeed, the fine structures of the temporal profile as well as the statistical fluctuations are finely reproduced by the calculations. As the temporal MLM profiles are very similar at 1ω and 3ω, the effect of frequency conversion is not numerically investigated, for they represent little interest in this part. However, in the next part, the influence of temporal incoherence on the spatial characteristics of the beam is investigated and simulated at both wavelengths.

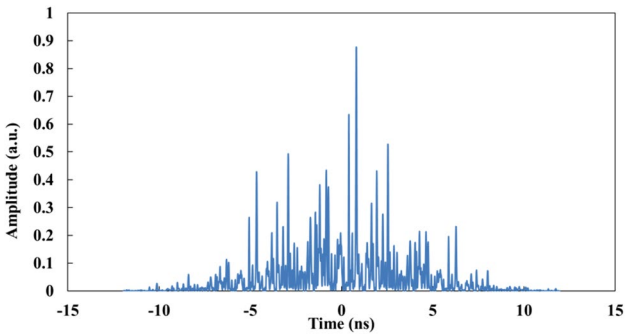

Fig. 11 Numerical simulation of a possible MLM temporal profile at 1ω

4 Spatiotemporal dynamics of unstable resonators with variable reflectivity mirror

In this part, the interest of the study is the spatial characteristics of the laser described in Fig. 1. Here, the streak cameras are used as a diagnostic for spatiotemporal dynamics in the far field [20]. Again, the dynamic range and the intensity-dependent time resolution of the streak camera have been taken into account in order to avoid space charge and accumulative saturation effects.

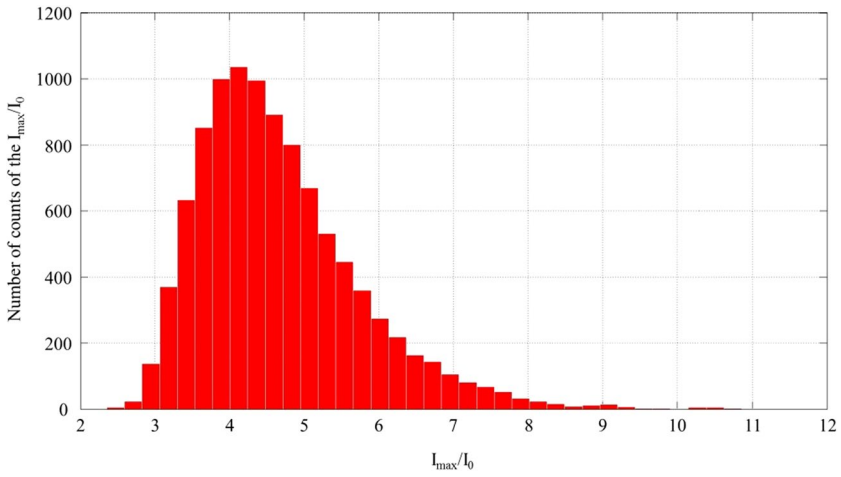

Fig. 12 Number of counts of the ratio of the value of the highest spike I_{max} on the maximum I_0 of their equivalent SLM pulse over 10,000 simulated 1ω MLM pulses

4.1 Experimental evidence of spatial incoherence in the focal plane

The object of this part is to study the spatiotemporal dynamics in the MLM regime at the far field. The effect of frequency conversion is also investigated. The extraction of high energy in such Nd:YAG laser cavity results in a beam of poor spatial quality. Previous studies showed an alteration of the beam at the near field when a laser works in an almost-stable configuration [3, 4]. In order to observe the differences observed in the spatial profiles between the SLM and the MLM regimes at the two wavelengths, the CCD camera has been positioned at the far field, in the focal plane of the 8-m focusing lens. Time-integrated acquisitions of the sub-millimetric focal spots are reported in Fig. 13. One can note that the feet of the focal spots are quite intense due to thermal-induced aberrations. The experimentally measured radiuses at 1/e of the Gaussian part of the focal spots are reported in Table 1 for both wavelengths at 1ω and 3ω. Then, the equivalent surface S_{eq} of each beam is calculated as the ratio of the sum of the gray levels of all the pixels of the image after removing the background noise on the maximum value of the image [21] with the knowledge of the size of a pixel. The results of these measurements are reported in Table 1.

Table 1 Equivalent surfaces and radiuses of the focal spots in both SLM and MLM regimes at 1ω and 3ω

	SLM	MLM
$S_{eq}^{1\omega}(\mathrm{mm}^2)$	1.16	1.32
$r^{1\omega}(\mu\mathrm{m})$	480	510
$S_{eq}^{3\omega}(\mathrm{mm}^2)$	0.467	0.718
$r^{3\omega}(\mu\mathrm{m})$	265	320

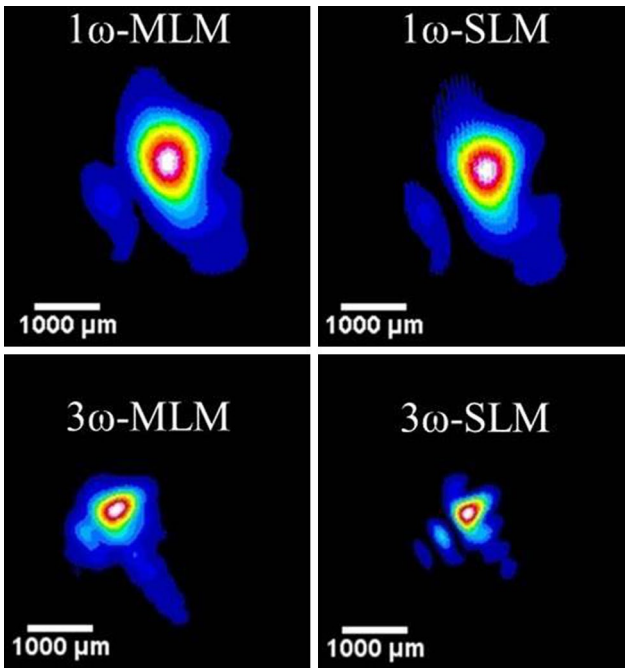

Fig. 13 Time-integrated acquisitions of the beam profile in the far field for both MLM and SLM regimes at 1ω as well as at 3ω

At 1ω (respectively 3ω), the equivalent surface of the MLM beam is 12 % (respectively 35 %) larger than the SLM spot. The radius of the MLM focal spot is 6 % (respectively 21 %) larger than the SLM one. The results clearly show that MLM far-field profiles are systematically larger than the SLM ones. These increases in the beam equivalent surfaces are supposed to arise from spatial incoherence induced by longitudinal mode beating.

In order to quantify the spatiotemporal dynamics that the beam undergoes, time-resolved streak camera acquisitions made at the far field are reported in Fig. 14 for the four configurations. Inserts of Fig. 14 show a zoom of the streak camera images in order to emphasize the spatiotemporal dynamics. The slits of the two streak cameras are positioned in the focal plane so as to enclose the barycenter of the spots: The slits are centered on the focal spot. The caliber of the 1ω streak camera is 56 ps/mm, and the caliber of the 3ω streak camera is set to 33 ps/mm. The slit of both streak cameras is opened by 100 µm, which is coherent with the radiuses of the spot of Table 1. The spatial coordinate (parallel to the slit) is in the vertical direction in the images of Fig. 14. The spatial resolution of each image is about 20 µm (i.e., 2.5 µrad with the 8 m focal length). For these images, the magnifying power induced by imagery has been taken into account. At both wavelengths, in the SLM regime, no effect of spatiotemporal coupling is observed. The beam profile on the spatial coordinate does not evolve with time. However, MLM acquisitions show clear evidences of spatiotemporal coupling during the pulse. In the inserts of Fig. 14, one can note the almost instantaneous displacements of the focal spots toward the vertical direction parallel to the slit. In the four images, the time-integrated radiuses of the profiles are equal to those of Table 1. However, short-time average radiuses measured in the MLM regime on the streak images of Fig. 14 are smaller.

The maximum displacements of the barycenter and the mean position corresponding to zero of each MLM spot are reported in Fig. 15 for both 1ω (Fig. 15a) and 3ω (Fig. 15b) MLM acquisitions. At 1ω, the measured displacement corresponds to a maximum angular deviation of 10 µrad, whereas it is 30 µrad at 3ω. One can note that the spatiotemporal displacements are more pronounced at 3ω than at 1ω.

The same measurements have been performed with the slit in the perpendicular direction on the spots, and the

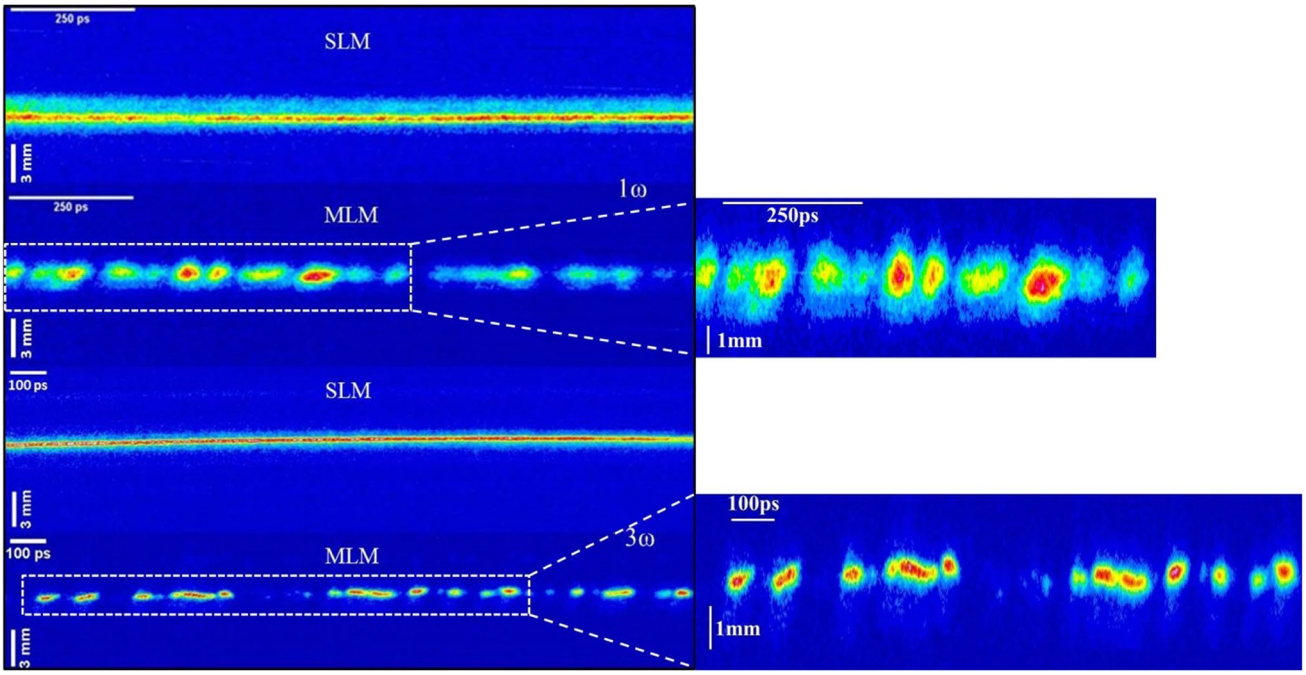

Fig. 14 Spatiotemporal acquisitions of the beam in the different configurations. The vertical coordinate parallel to the slit stands for the spatial coordinate. The horizontal coordinate perpendicular to the slit stands for the time coordinate. *Inserts* show a zoom of the streak camera images

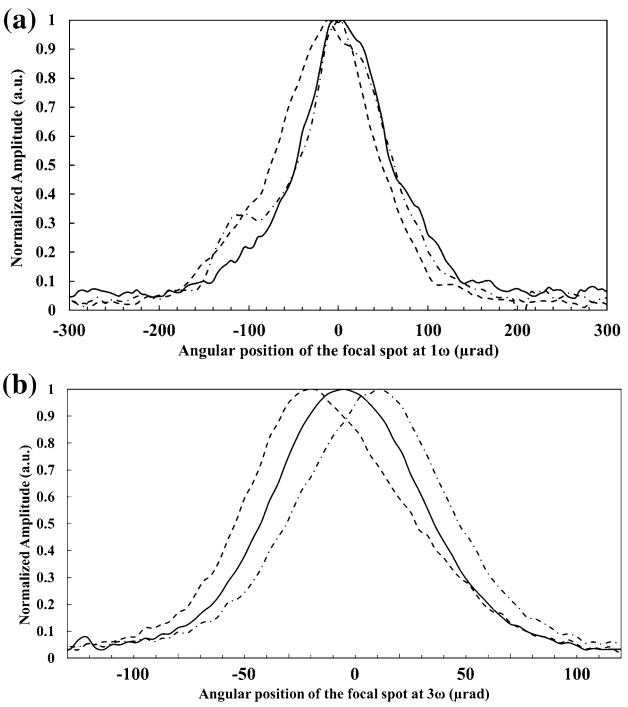

Fig. 15 Angular position in the focal plane of some spikes measured on the images of Fig. 12 for both 1ω (**a**) and 3ω (**b**) MLM acquisitions. Only the spikes corresponding to the maximum angular displacement are reported

same displacements are obtained. Thus, the spatiotemporal dynamics do not depend on the direction of observation. The enhancement of the surface seen on the CCD images of Fig. 13 in the MLM regime is a consequence of this spatiotemporal dynamics. Indeed, the geometrical focal spot, which is smaller, is convolved with a time-dependent angular displacement that enhances the measured time-integrated equivalent surface. A systematical error is thereby made when measuring time-integrated spot sizes in the MLM regime at the far field. The angular displacement induces an error in surface which depends on the focal length that is used in the experiments.

4.2 Discussion

In order to explain the observed spatiotemporal coupling in the MLM regime, different hypotheses were confronted. First, the absence of any dispersive optical component such as an optical grating or a prism on the propagation of the laser pulses suggests that the source of the phenomenon is not linked to spectral optical smoothing. The effect we considered in order to explain the tendency is the generation of nonlinear Kerr effect in the amplifiers. A spatial profile of poor quality coupled to high spikes in power could bring enough phase distortion so

as to induce such spatial incoherence. Moreover, nonlinear Kerr effect does not depend on any direction as it would be generated randomly in this case. This hypothesis is now compared with the predictions of a numerical simulation. In this theoretical approach, the geometry of the cavity is not taken into account and thus does not affect the results.

The simulated 1ω temporal profile described in the previous part is propagated with a transversal coordinate. At the output of the laser, the beam is supposed to be super-Gaussian on the spatial dimension. Realistic random modulations are implemented in the spatial profile as the beam of this type of laser exhibits a poor spatial quality (cf. Fig. 13). Then, we will consider the coefficient of the nonlinear part of the refractive index of Nd:YAG of $n_2 = 7.5.10^{-20}$ m^2/W [22]. The integral of the nonlinear phase B accumulated in the four Nd:YAG rods is calculated as [18]:

$$B = \frac{2\pi L}{\lambda} n_2 I,$$

where $\lambda = 1064$ nm is the fundamental wavelength of the laser, $L = 4l \approx 60$ cm is the total length of the four Nd:YAG rods with $l = 15$ cm, and I is the irradiance. In this calculation, we made the assumption that the four Nd:YAG rods play the same role in building the nonlinear phase. This hypothesis leads to an overestimation of B. The more the beam is modulated both in space and time, the more it will suffer from nonlinear Kerr effect. The beam with its nonlinear spatial phase is then propagated through a focusing lens of an 8-m focal length. The focal spot of the beam is calculated thanks to a Fourier transform of the spatial coordinate. The results of the simulation are reported in Fig. 16. In Fig. 16a, the entire two-dimensional image of the focal spot is reported. The angular positions of three short-time average spots are reported in Fig. 16b, c. The angular shift measured between the dashed curve and the dash-dotted curve is 8 µrad, which is in the same order of magnitude than the 10 µrad measured experimentally. Moreover, one can note in Fig. 16b that this shift is conjugated with a narrowing of the spatial profile of the spot. However, the measured time-integrated diameter is in agreement with the experimental value. This means that the spatial modulations implemented in the beam in the calculation are not too rough. The displacement as well as the narrowing seen on the simulation is a consequence of the accumulation of nonlinear spatial phase. The observed shift and narrowing depend on the magnitude of the spikes and on the spatial modulation. The combination of these two parameters makes it possible for the growth of instabilities that traduces spatial incoherence [12]. This simulation thus allows us to propose an interpretation of the observed experimental tendency and shows a good correlation with the displacement measured in Fig. 15a. Similar calculations

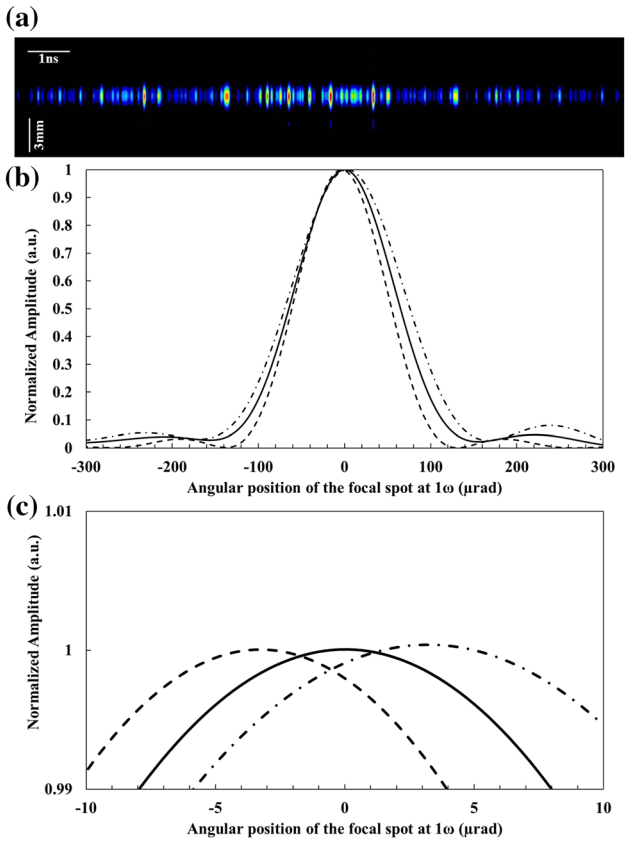

Fig. 16 **a** Simulated two-dimensional image of the focal spot at 1ω. The entire temporal length of the pulse is presented. **b** Representation of the angular position of different spots in the focal plane. **c** Zoom on the maximum of these spots

have been made without considering nonlinear Kerr effect, and no angular shift is observable.

The same 1ω beam will now undergo frequency conversion before being focused. The thicknesses of the two crystals are 25 mm, and their diameters are 12.7 mm. The second-harmonic generator crystal is a type I KDP, and the third-harmonic generator crystal is a type II KDP. Nonlinear Kerr effect is supposed to be negligible in the crystals. Diffraction effects as well as walk-off are taken into account in the propagation of the beam through the crystals. Each crystal has been numerically cut into slices in order to use a split and step method with successive Fourier transforms. Coupled equations described in ref. [18] are resolved in two dimensions with the slowly varying envelop approximation for each slice. Then, the focal spot of the beam is calculated as the Fourier transform of the transverse coordinate of the near field. The results of the simulation are reported in Fig. 17. In Fig. 17a, the entire two-dimensional image of the focal spot is reported. The angular positions of three short-time average spots are reported in Fig. 17b, c. The angular shift measured between the dashed curve and the dash-dotted curve is 14 µrad, which is larger than in the 1ω

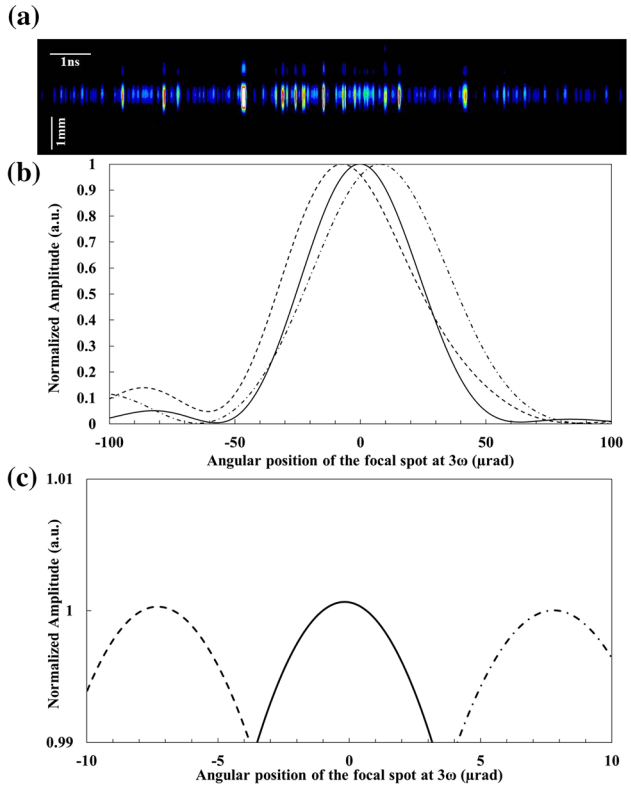

Fig. 17 **a** Simulated two-dimensional image of the focal spot at 3ω. The entire temporal length of the pulse is presented. **b** Representation of the angular positions of different spots in the focal plane. **c** Zoom on the maximum of these spots

simulation. Again, these shifts are conjugated with slight variations of the diameter of the spots. This value does not exactly correspond to the experimental observations where an angular displacement of 30 μrad is measured at 3ω, but the calculated shifts are in the good order of magnitude. Thus, this simulation allows us to propose an interpretation of the observed experimental tendency, but does not really show a good quantitative correlation at 3ω with the images of Fig. 15.

As the 3ω beam is most affected by spatial incoherence, the frequency conversion can be supposed to be responsible for most of the obtained angular shift. Previous theoretical works predict possible phase distortions [23] or angular shift of a divergent beam [24, 25] during sum-frequency mixing. These effects are sensitive to the direction of the polarization at the output of the crystal, for they depend on harmonic generation mechanisms and nonlinear propagation. However, the previous observations show that at least two perpendicular directions are affected. Therefore, these phenomena cannot be the cause of our observations. Other works show evidence of dispersion in KDP crystals as great as −1.1 mrad/nm in a type II KDP third-harmonic generator [26, 27]. Again, this would induce unidirectional shifts at 3ω, and it is not the case. Moreover, the wavelength is not shifting as much as it would be necessary during a MLM pulse for the obtained few tens of μrad [17].

5 Conclusion

In the present work, we have investigated the incoherent nature of MLM pulses at the output of a commercial Nd:YAG Q-switched laser in both the temporal and the spatial domains at 1ω and 3ω. The measurement of the spectral width of the pulses has allowed the definition of the bandwidth of the instruments used for the temporal acquisitions. As a result, a minimum bandwidth of 30 GHz is required in order to fully resolve the MLM temporal profiles. In this configuration, for both wavelengths, intensity spikes contained within the pulse can be as short as a few tens of picosecond, corresponding to the shortest time the cavity can generate. At 1ω (respectively 3ω), the magnitude of these spikes is on the average around 4.6 (respectively 3.7) times higher than the maximum of the equivalent SLM pulse and can reach a maximum value of ten times the maximum of the equivalent SLM pulse. This strong temporal incoherence is resulting in spatiotemporal coupling in the focal plane. As a consequence, the equivalent surface of the focal spots of MLM pulses is larger than the SLM ones for both wavelengths. The direct observation of this behavior has been possible by means of picosecond streak cameras. At 1ω (respectively 3ω), an almost instantaneous displacement of 10 μrad (respectively 30 μrad) is observed on the streak images of MLM focal spots. These measurements are clear evidences of spatial incoherence in the focal plane. This means that a process occurs in the propagation of the laser beam leading to the translation of temporal incoherence into spatial incoherence. In this study, we propose that the occurrence of nonlinear Kerr effect in the Nd:YAG amplifiers during the buildup of the pulse may be the reason of the observed spatiotemporal dynamics. This hypothesis is confronted to numerical calculations, but leads to qualitative-only interpretations of the observed tendency. Additional experiments involving different cavity setups with different frequency conversion architectures may be performed as far as MLM pulses are involved. Moreover, a specific analysis of the output of the doubling crystal may lead to a better understanding of the behavior of the UV output. This study finally demonstrates that working with MLM pulses without bringing into operation the proper metrology may be hazardous, especially in light–matter interaction experiments such as laser-induced damage test. For some application, it might thus be necessary to work on an injection seeder that avoids spatial incoherence while producing temporally incoherent pulses.

Acknowledgments The authors would like to thank Jérôme Ribolzi for his technical support bringing into operation the streak cameras and Jean-Luc Dubois for fruitful discussions about the interpretation of streak camera acquisitions.

References

1. S. DeSilvestri, P. Laporta, V. Magni, O. Svelto, IEEE J. Quantum Electron. **24**, 1172–1177 (1988)
2. K.J. Snell, N. McCarthy, M. Piché, P. Lavigne, Opt. Commun. **65**, 050377 (1988)
3. A. Caprara, G.C. Reali, Opt. Lett. **17**, 060414 (1992)
4. G. Ansett, M. Nittmann, A. Borsutzky, R. Wallenstein, Appl. Phys. B **76**, 833–838 (2003)
5. Y.K. Park, G. Giuliani, R.L. Byer, Opt. Lett. **5**, 030096 (1980)
6. I.A. Rahn, R.L. Farrow, R.P. Lucht, Opt. Lett. **9**, 060223 (1984)
7. R.L. Farrow, L.A. Rahn, J. Opt. Soc. Am. B **2**, 060903 (1985)
8. O. Kinrot, I.S. Averbukh, Y. Prior, Phys. Rev. Lett. **75**(21), 3822 (1995)
9. D. Huang, E.A. Swanson, C.P. Lin, J.S. Schuman, W.G. Stinson, W. Chang, M.R. Hee, T. Flotte, K. Gregory, C.A. Puliafito, J.G. Fujimoto, Science **254**, 1178 (1991)
10. R.H. Lehmberg, S.P. Obenschain, Opt. Commun. **46**, 27 (1983)
11. D. Véron, H. Ayral, C. Gouedard, D. Husson, J. Lauriou, O. Martin, B. Meyer, M. Rostaing, C. Sauteret, Opt. Commun. **65**, 010042 (1988)
12. J. Garnier, L. Videau, C. Gouédard, A. Migus, J. Opt. Soc. Am. B **15**, 112773 (1998)
13. Gratings spectrometer. Patent n° 13 57812
14. D.J. Bradley, B. Liddy, W.E. Sleat, Opt. Commun. **2**, 080391 (1971)
15. D.J. Bradley, S.F. Bryant, J.R. Taylor, W. Sibbett, Rev. Sci. Instrum. **49**, 020215 (1978)
16. W. Friedman, S. Jackel, W. Seka, J. Zimmermann, Proc. SPIE **97**, 544–548 (1976)
17. G. Ansett, R. Wallenstein, Appl. Phys. B **79**, 827–836 (2004)
18. R.W. Boyd, *Nonlinear Optics* (Elsevier, Amsterdam, 1992)
19. R. Diaz, M. Chambonneau, R. Courchinoux, P. Grua, J. Luce, J.-L. Rullier, J.-Y. Natoli, L. Lamaignère, Opt. Lett. **39**, 030674 (2014)
20. C. Gouedard, D. Husson, C. Sauteret, F. Auzel, A. Migus, J. Opt. Soc. Am. B **10**, 122358 (1993)
21. A. Stratan, A. Zorilla, L. Rusen, G. Nemes, Opt. Eng. **53**(12), 122513 (2014)
22. A. Tomita, Appl. Phys. Lett. **34**, 070463 (1979)
23. A.V. Smith, M.S. Bowers, J. Opt. Soc. Am. B **12**, 010049 (1995)
24. J. Garnier, J. Math. Phys. **42**, 041612 (2001)
25. J. Garnier, J. Math. Phys. **42**, 041636 (2001)
26. R.S. Craxton, S.D. Jacobs, J.E. Rizzo, R. Boni, IEEE J. Quantum Electron. **17**, 091782 (1981)
27. M.D. Skeldon, R.S. Craxton, T.J. Kessler, W. Seka, R.W. Short, S. Skupsky, J.M. Soures, IEEE J. Quantum Electron. **28**, 051389 (1992)